Journal of Non-Newtonian Fluid Mechanics 199 (2013) 1–11

Contents lists available at SciVerse ScienceDirect

Journal of Non-Newtonian Fluid Mechanics

journal homepage: http://www.elsevier.com/locate/jnnfm

Computational study of viscoelastic effects on liquid transfer during gravure printing

J. Alex Lee [a], Jonathan P. Rothstein [b], Matteo Pasquali [a,c,*]

[a] Department of Chemical and Biomolecular Engineering, Rice University, Houston, TX 77005, USA
[b] Department of Mechanical Engineering, University of Massachusetts – Amherst, Amherst, MA 01003, USA
[c] Department of Chemistry, Ken Kennedy Institute for Information Technology, The Smalley Institute for Nanoscale Science & Technology, Rice University, Houston, TX 77005, USA

ARTICLE INFO

Article history:
Received 31 January 2013
Received in revised form 22 May 2013
Accepted 23 May 2013
Available online 31 May 2013

Keywords:
Viscoelasticity
Gravure
Filament stretching
Liquid bridge
Finite element

ABSTRACT

High speed roll-to-roll coating and printing are important in both classical and novel processes, e.g., in the emergent flexible electronics industry. Gravure in particular is attractive for its application to printing as well as its high quality and throughput in coating continuous thin films. Despite its long standing use, gravure is still poorly understood especially in the liquid transfer regime and when the coating liquid has a complex rheology. As with any coating flow, the dynamics are governed by many complex phenomena including free surfaces, (de)-wetting, and non-Newtonian rheology; these present observational, modeling, and computational challenges. Accordingly, modeling and computational work are usually limited by the level of detail in describing the physical phenomena. In this work, we compute the influence of viscoelasticity on the transfer of polymer solutions in an idealized gravure process: the liquid is held between a cavity and a flat disk that moves away at a constant velocity, with pinned contact lines on both the disk and cavity. Our computations show that when the disk separation velocity is sufficiently high as measured by the Weissenberg number—i.e., the consequent strain rate in the liquid bridge is high compared to the rate of polymer relaxation—large elastic stresses are activated at early times and induce an adverse drainage into the cavity. Gravity or other forces eventually overwhelm this elastic drainage at later times when stretching dynamics decay in importance. When gravitational and elastic drainage act in concert, they compete with the viscous forces that promote liquid transfer; this competition manifests as an optimum disk velocity for maximal liquid transfer. With the appropriate scaling, we find that the optimal disk velocities over a range of parameters reduce to an optimal Weissenberg number of about 0.1, which agrees well with experiments in the literature.

1. Introduction

Gravure is commonly employed as a high speed roll-to-roll coating or printing (patterned coating) method in a variety of products including magazines and packaging. More recently, it is being investigated as a potential route for high throughput manufacturing of high tech devices such as printed electronics [1] and solar cells [2]. Many coating liquids of relevance contain particles and macromolecules, or are otherwise structured at the nanoscale. Such liquids exhibit complex rheological behavior such as shear thinning, extension hardening, and viscoelasticity. The role of complex rheology in gravure coating is still poorly understood, and we aim to elucidate the relevant phenomena by computational modeling.

In the typical gravure process, a pattern of cavities (gravure cells) engraved on a cylindrical roller (the gravure roll) constitutes the liquid delivery mechanism and is shown schematically in Fig. 1. The gravure cells are filled by partially immersing the rotating gravure roll in a bath, then doctoring off the excess liquid with a blade. The liquid adheres to the web when the gravure roll is pressed onto it, and the rolling action results in the formation of a stretching and shearing liquid bridge between the cavity and web. Liquid transfer is completed by the combination of de-wetting from the cavity wall and the instability-driven capillary break-up of the liquid bridge.

Depending on the process configuration, the liquid bridge may experience a strong shearing motion—not to be confused with shear flow within the liquid—for example in the extreme case of reverse operation where the gravure roll rotates counter to the web (counter-clockwise in Fig. 1). The effects of such shearing motions during gravure roll separation have been investigated both experimentally [3,4] and computationally [5–8]. In cases where the shearing motion is small, e.g., in Fig. 1 when $U_{web} \approx U_{roll}$ for

* Corresponding author at: Department of Chemical and Biomolecular Engineering, Rice University, Houston, TX 77005, USA. Tel.: +1 713 348 5830.
E-mail address: mp@rice.edu (M. Pasquali).

0377-0257/$ - see front matter © 2013 Elsevier B.V. All rights reserved.
http://dx.doi.org/10.1016/j.jnnfm.2013.05.005

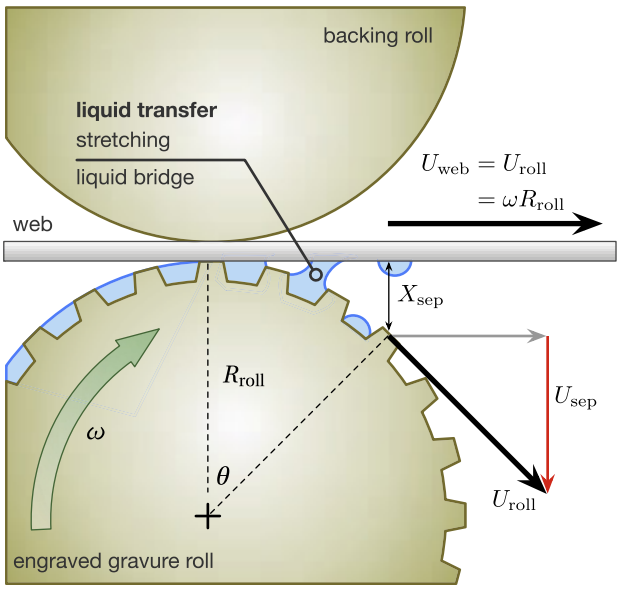

Fig. 1. Schematic of the generic gravure printing process.

$\theta \ll 1$, the liquid bridge may be approximated as axisymmetric and the stretching as uniaxial. A growing number of works takes this approach to investigate liquid transfer efficiency using filament-stretching apparatuses [9–11] and analogous computations [12–16].

There is a substantial body of literature concerning the dynamics of stretching liquid bridges and jets dating back to the pioneering works of Rayleigh [17] and Plateau [18]. The dynamic evolution of the free surface profile up to the instability-driven break-up event is particularly relevant to the gravure liquid transfer process in describing the partition of liquid on the cavity and web when the liquid does not completely de-wet from the cavity walls. Theoretical works have shown, for example, that the evolution of free surface profiles become self-similar near break-up for viscous liquids with and without inertia [19–21] and even for viscoelastic liquids [22]. A consideration of equilibrium liquid bridge configurations and stability [23] can also be instructive in the context of the quasi-equilibrium limit of stretching dynamics [24,25], where surface tension and gravity dominate viscous and inertial forces.

Following the introduction of extensional rheometry [26–29], several computational investigations of stretching liquid bridge dynamics have appeared using diverse numerical strategies and non-Newtonian rheological models [30–37]. These studies held liquid between two flat disks and pinned the contact lines—conditions necessary for extensional rheometry. In the context of gravure, one of the disks must be replaced with a cavity and the contact lines may move [10,12–16]. Indeed, experiments have shown the role of de-wetting—i.e., the solid-liquid interaction between the gravure roll and the coating liquid—to be important in determining the transfer of liquid [10]. Computational studies have taken similar approaches, characterizing the solid-liquid interfacial properties parametrically as static contact angles [13,14,16].

Moving contact lines, however, present many modeling and computational challenges, especially for viscoelastic rheologies. To begin, the details of the physics governing contact line dynamics are poorly understood, as illustrated by the paradox arising between the moving contact line and the no-slip condition at solid-liquid interfaces [38]. While numerous theories have been put forth (Ref. [39] for a recent review), a common modeling strategy is to relax the no-slip condition at or near the contact line using Navier's slip law, as has been done in the computational investigations for gravure liquid transfer cited above.

Viscoelasticity, which arises in many polymeric liquids, has only recently been explored experimentally in the context of gravure [9]. While viscoelasticity has been incorporated in several computational studies of stretching liquid bridges held between flat disks with pinned contact lines [31,36,40], there have not yet been any such studies with cavity or moving contact lines characterizing the gravure process. To our knowledge, computation of non-Newtonian liquids in gravure liquid transfer have been limited to purely viscous non-Newtonian rheological models [15,37]. This limitation is partly due to the compounded difficulty of modeling moving contact lines with current methods for modeling viscoelasticity, and there are few instances of computing generally (de)-wetting flows of viscoelastic liquids [41–43].

The logical first step in modeling liquid transfer is to analyze the flow in the presence of a cavity but with pinned contact lines. The latter simplification alleviates the aforementioned uncertainties associated with modeling the interfacial physics, especially in concert with complex rheologies (i.e. viscoelasticity). This approach does not appear in the literature though, presumably because the role of de-wetting is expected to be dominant. In fact, recent experiments by Sankaran and Rothstein [9] have demonstrated that in certain regimes of material and process parameters, the liquid remains pinned to the outer corner of the cavity. Under this condition of pinned contact line, viscoelasticity either impedes or enhances liquid transfer depending on whether the experiment was inverted, indicating that gravity plays an important role. Furthermore, activation of elastic effects—though only when in concert with gravity—resulted in the observation of an optimal coating speed for maximum liquid transfer.

Here, we examine computationally the effects of viscoelasticity on liquid transfer during a model gravure process with the simplification of pinned contact line. Computations are carried out under the same conditions as the experiments of Sankaran and Rothstein [9]—namely with matching system geometry and similar liquid properties. Results agree quantitatively with experiments for Newtonian liquids and weakly elastic liquids. The findings and conclusions from the experiments are extended by exploring a larger parameter space.

2. Problem formulation and methods

2.1. Description of physical system

The model gravure process is an axisymmetric stretching liquid bridge over a trapezoidal cavity, shown schematically in Fig. 2. Liquid is held between this cavity and a disk initially L_0 from the cell,

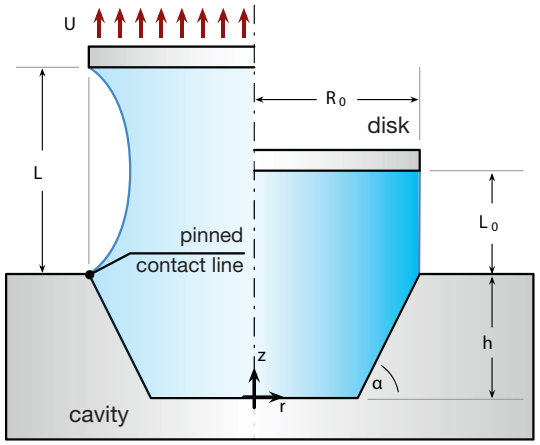

Fig. 2. Schematic of the axisymmetric model gravure system. Geometric parameters are fixed: wall angle $\alpha = 75°$, initial cavity depth $h/L_0 = 4/3$, and initial liquid bridge aspect ratio $L_0/R_0 = 0.3$.

and is pulled from the cavity by action of lifting the disk with velocity U, roughly corresponding to coating speed U_{sep} (Fig. 1). The liquid remains pinned at the gravure cell perimeter and the disk corner, both with radius R_0.

At steady operation, the web in Fig. 1 translates tangent to the gravure roll from the point of contact, with velocity assumed equal to the linear velocity of the roll surface $U_{roll} = \omega R_{roll}$ where ω and R_{roll} are the angular velocity and the radius of the gravure roll. The angular displacement of a cavity on the roll at time t after contact with the web is $\theta(t) = \omega t$, and so the rate of separation between the cavity and point of contact on the web is $U_{sep} = \omega R_{roll} \sin \omega t$. For $\theta_s = \omega t \ll 1$, the small angle approximation yields $U_{sep} \approx \omega^2 R_{roll} t$ such that in the axisymmetric model, the cavity translates downward with constant acceleration $a = \omega^2 R_{roll}$ away from a stationary disk.

The case where the web conforms to the backing roll (with the same radius as the gravure roll in Fig. 1), can be modeled with cavity and disk that are accelerating away from each other with absolute accelerations $\pm a$ and relative acceleration $2a$. Because of inertia, this situation is distinct from one where the cavity translates downward with acceleration $2a$ away from a stationary disk; the two situations are only equivalent in the quasi-steady limit of vanishing inertia. A simpler model for the separating motion is that of constant velocity, for which only the relative velocity matters even when inertial effects are important (except during the brief initial acceleration from rest).

Previous works using the axisymmetric liquid bridge model for gravure printing [9,10,12–16] have adopted this latter constant velocity model, and we therefore focus on this approach. The constant acceleration and constant velocity experiments are not equivalent, however, except in the further restrictive quasi-equilibrium limit (negligible dynamics). Nevertheless, our preliminary experiments (unpublished) showed that results were qualitatively similar for constant acceleration versus constant velocity experiments. We confirmed this finding by computation for a few test cases near the quasi-steady limit, and refer to the Supplementary materials for the results and their discussion.

2.2. Governing equations and numerical method

The governing equations and numerical method parallel those of previous works [36,44,45] and are only briefly summarized here for convenience. The incompressible flow of Newtonian and viscoelastic liquids is governed by the conservation equations for momentum and mass

$$\rho\left(\frac{\partial \mathbf{v}}{\partial t} + \mathbf{v}\cdot\nabla\mathbf{v}\right) = \nabla\cdot\mathbf{T} + \rho\mathbf{g} \tag{1}$$

$$0 = \nabla\cdot\mathbf{v} \tag{2}$$

with fluid velocity $\mathbf{v}$, the Cauchy stress tensor $\mathbf{T}$, and gravity $\mathbf{g}$. The extra stress comprises purely viscous and elastic parts $\boldsymbol{\tau}_v$ and $\boldsymbol{\tau}_e$ such that

$$\mathbf{T} = -p\mathbf{I} + \boldsymbol{\tau}_v + \boldsymbol{\tau}_e \tag{3}$$

where p is the pressure. The viscous part is modeled by Newton's constitutive law

$$\boldsymbol{\tau}_v = \eta_s[\nabla\mathbf{v} + (\nabla\mathbf{v})^{\mathrm{T}}] \tag{4}$$

with η_s the Newtonian or solvent viscosity.

The elastic contribution to the stress is modeled within the framework of the general conformation tensor based constitutive equations [44,45]. The dimensionless conformation field $\mathbf{M}$ embodies the microstructural details of the polymer in solution [45–48] by averaging the molecular stretch and orientation states in a continuum representation. We choose the FENE-P constitutive model based on the finitely extensible nonlinear elastic (FENE) dumbbell model for microstructured liquids. The free energy associated with the conformation state $a(\mathbf{M})$ for a FENE-P dumbbell is [45]

$$a = \frac{3G}{2\rho}(b-1)\ln\frac{b-1}{b-\frac{\mathrm{tr}\,\mathbf{M}}{3}} \tag{5}$$

yielding the elastic contribution to the stress [45]

$$\boldsymbol{\tau}_e = 2\rho(\mathbf{M}-\mathbf{I})\cdot\frac{\partial a}{\partial \mathbf{M}} = G\frac{b-1}{b-\frac{\mathrm{tr}\,\mathbf{M}}{3}}(\mathbf{M}-\mathbf{I}) \tag{6}$$

where b is the finite polymer extensibility parameter and G is the elastic modulus, or the ratio of polymer viscosity to relaxation time. Hereafter, the polymer viscosity is put in terms of the solvent viscosity ratio β and the zero shear viscosity $\eta_0 = \eta_s + \eta_p$ so that

$$G = \frac{\eta_p}{\lambda} = \frac{(1-\beta)\eta_0}{\lambda} \tag{7}$$

The constitutive model is completed by specifying the evolution equation for the conformation field

$$\frac{\partial \mathbf{M}}{\partial t} + \mathbf{v}\cdot\nabla\mathbf{M} - \mathbf{M}\cdot\nabla\mathbf{v} - \nabla\mathbf{v}^T\cdot\mathbf{M} = -\frac{1}{\lambda}\left(\frac{b-1}{b-\frac{\mathrm{tr}\,\mathbf{M}}{3}}\mathbf{M} - \mathbf{I}\right) \tag{8}$$

where the right hand side describes the FENE-P model-specific relaxation toward the equilibrium state (in this case when $\mathbf{M} = \mathbf{I}$), and the left hand side is the upper convected derivative common to any constitutive model for which the conformation deforms affinely with the flow.

The conserved quantities require boundary conditions on three boundaries, namely the interfaces with the cavity, the moving disk, and the surrounding air. The axisymmetric domain additionally requires symmetry conditions along the axis. The conformation tensor evolution equation is hyperbolic and therefore requires conditions only at inflow boundaries, of which there are none in this system. Boundary conditions for the momentum equations follow.

Along the symmetry axis, the zero-shear and no-penetration conditions hold

$$0 = \mathbf{e}_r\cdot\mathbf{v} \tag{9}$$

$$0 = \mathbf{e}_z\mathbf{e}_r : \mathbf{T} \tag{10}$$

where $\mathbf{e}_r$ and $\mathbf{e}_z$ are unit basis vectors.

For simplicity we assume the surrounding air is inviscid, so the free surface requires only a normal stress balance given by the Laplace equation

$$\mathbf{n}\cdot\mathbf{T} = (-p_{amb} + \kappa\sigma)\mathbf{n} \tag{11}$$

where $\mathbf{n}$ is the outward unit boundary normal, κ denotes twice the local mean curvature of the free surface, σ is the interfacial tension, and p_{amb} is the prescribed ambient pressure,

Because the contact line is pinned, the fluid velocity on the moving disk and cavity are specified by the no-slip and no-penetration conditions. Consequently, the contact angle is unconstrained and no additional physics are required. The separation velocity is applied from rest with a brief acceleration so that the initial condition corresponds exactly to the equilibrium conditions $\mathbf{v} = \mathbf{0}$ and $\mathbf{M} = \mathbf{I}$. As long as the initial transient is sufficiently brief, the boundary condition can be applied to either the cavity or the disk without appreciably changing the results (see Supplementary materials).

The conservation equations for 2D axisymmetric flow are solved by the finite element method using an ALE formulation to handle domain deformation due to free surfaces; the evolving finite element mesh positions obeying an elliptic equation are computed together with the solution of the field equations [49,50]. The

moving free surface is coupled to the momentum equations by specifying kinematic (i.e. impenetrability) conditions on the boundary interface

$$0 = \mathbf{n} \cdot (\mathbf{v}_s - \dot{\mathbf{x}}_s) \tag{12}$$

where $\dot{\mathbf{x}}_s$ and $\mathbf{v}_s$ are the mesh velocity and fluid velocity at the free surface. The moving solid wall boundary position is specified independently as the time-integral of the imposed velocity U.

We adopt the DEVSS-TG formulation [44] to improve numerical properties of the solution algorithm. An additional field variable

$$\mathbf{L} = \nabla\mathbf{v} - (\nabla \cdot \mathbf{v})\mathbf{I}/\mathrm{tr}\ \mathbf{I} \tag{13}$$

provides a c_0-continuous and divergence-free representation of the velocity gradient used to modify the coupling between the conformation and momentum field equations. Replacing the $\nabla\mathbf{v}$ terms with $\mathbf{L}$ in Eq. (8) ensures volume-conservative deformations of the conformation tensor [44]. The viscous stress term is stabilized by modifying Eq. (4):

$$\boldsymbol{\tau}_v = \eta_s[\mathbf{L} + \mathbf{L}^{\mathrm{T}}] + \eta_a[\nabla\mathbf{v} + (\nabla\mathbf{v})^{\mathrm{T}} - \mathbf{L} - \mathbf{L}^{\mathrm{T}}] \tag{14}$$

where η_a is a numerical parameter whose value is of the same order as η_s. The hyperbolic nature of the conformation evolution equation is addressed by SUPG stabilization [51].

The FEM-discretized equations are integrated in time using the fully implicit second order Adams-Moulton method (the trapezoid rule) with variable time steps [36,52].

Finally, the resulting algebraic equations are solved with Newton's method using a combination of analytic and numerical Jacobian. Each Newton step is solved by LU decomposition using a frontal algorithm parallelized by OpenMP and executed on up to 12 processors in shared memory configuration.

2.3. Relevant parameters and definitions

Liquid transfer is computed as a function of the constant stretching velocity (disk velocity) U for Newtonian and FENE-P liquids. Experimental results are reported as the fraction ϕ of liquid removed from the cavity after break-up [9]. In our computations, this fraction is measured in terms of the liquid above the horizontal plane cutting the filament at the pinch point (region of local minimum radius) $\varsigma = r_{\mathrm{pinch}}/R_0$. It is possible in certain parameter regimes for two pinch points to develop, in which case the filament breaks up at both to produce a free droplet. In gravure, such a droplet may fall back toward the gravure roll or onto the substrate (the latter resulting in the misting defect) depending on the direction of gravity [9]. The droplet volume is assumed to ultimately be removed from the cavity, and the computed measurement of liquid transfer is accordingly based on the pinch point closest to the cavity—the principal pinch point. The measurement is made when the thinnest pinch point (not necessarily the principal pinch point) satisfies $\varsigma < 10^{-2}$, which is found to be sufficiently close to break-up so that any further re-partitioning of liquid is insignificant.

Newtonian liquids are characterized by their viscosity η_0, density ρ, and surface tension σ. The relevant dimensionless numbers are the capillary number $\mathrm{Ca} = \eta_0 U/\sigma$, Ohnesorge number $\mathrm{Oh} = \eta_0/\sqrt{\rho\sigma R_0}$ and Bond number $\mathrm{Bo} = \rho g R_0^2/\sigma$. The sign of the Bond number specifies whether the cavity is on the bottom ($\mathrm{Bo} > 0$) or top ($\mathrm{Bo} < 0$). Fixing Bo and varying Oh corresponds in experiments to changing the concentration of short polymer in solution, which alters viscosity without appreciably affecting the density and surface tension. Experiments conducted at fixed Ca are equivalent for any liquids with the same Oh and Bo as long as the system's geometric aspect ratios are fixed.

The disk velocity may as well be reported as a Reynolds number $\mathrm{Re} = \rho U R_0/\eta_0 = \mathrm{CaOh}^{-2}$, which measures the importance of inertia, particularly at early process times when stretching dynamics dominate over capillary-driven thinning dynamics. Near the pinch point at late times, the relevant velocity scale is the capillary thinning velocity σ/η_0 (independent of disk kinematics), and therefore the relevant Reynolds number for describing capillary break up is $\overline{\mathrm{Re}} = \mathrm{Oh}^{-2}$ [20,32] (if $\mathrm{Oh} \ll 1$, the relevant characteristic velocity is the inertia-dominated capillary thinning velocity from which $\overline{\mathrm{Re}}_{\mathrm{cap}} = \mathrm{Oh}^{-1}$).

FENE-P liquids are characterized additionally by the solvent viscosity ratio $0 < \beta < 1$, polymer relaxation time λ, and extensibility parameter b. The relevant dimensionless numbers are the Deborah number $\mathrm{De} = \lambda\sigma/(\eta_0 R_0)$ and the Weissenberg number $\mathrm{Wi} = \lambda\dot{\gamma}$ where $\dot{\gamma}$ represents some characteristic process rate, e.g., a dimensionless stretching rate. The Deborah number is defined with respect to the viscous time scale $t_v = \eta_0 R_0/\sigma$ appropriate for liquids with high Oh where viscous forces dominate inertial forces. The limits $\mathrm{De} = 0$ and $\beta = 1$ correspond to Newtonian liquids. When Oh and Bo are fixed, De is varied by changing the relaxation time λ; this can be achieved in experiments by adding small amounts of a high molecular weight polymers of varying length. The solvent viscosity ratio can be altered in experiments by changing the concentration of the high molecular weight polymer additive.

Typical gravure cell sizes are in the range 10–100 μm engraved on rolls with radius $R_{\mathrm{roll}} \sim 100$ mm. A moderate-to-high linear web speed of $U_{\mathrm{web}} \sim 60$ m/min corresponds to roll angular velocity $\omega \sim 10$/s. Assuming a liquid bridge may stretch without breaking to lengths reaching 10 times the gravure cell size, the separation velocity may reach up to $U_{\mathrm{sep}} \sim 100$ mm/s. For a water based ink with $0.1 < \eta_0 < 1.0$Pa s, this corresponds to $\mathrm{Bo} \sim 0.001$, $\mathrm{Ca} \sim 1$, and $\mathrm{Oh} \sim 10$. In comparison, our system size adopted from [9] is scaled up to be experimentally feasible: lengths are scaled up keeping other parameters fixed so that the characteristic numbers are $\mathrm{Bo} \sim 1$, $\mathrm{Ca} \sim 1$, and $\mathrm{Oh} \sim 0.1$. Gravity and inertia thus play greater roles in our experiments than in a typical gravure operation.

3. Results

3.1. Newtonian liquids

To validate our approach, we compare in Fig. 3 the computed and experimental results for Newtonian liquids. The experiments were carried out using aqueous low molecular weight PEG solutions with cavity size $R_0 = 2.5$ mm ($\mathrm{Bo} = +1.2$) [9]. Over the range of PEG concentrations, the viscosity varies between $10 < \eta_0 < 60$ mPa s, corresponding to $0.03 < \mathrm{Oh} < 0.15$. The range of separation velocities $0.001 < U < 100$ mm/s corresponds to ranges for Ca and Re as indicated in Fig. 3. Agreement between the experiments and computations is excellent to within uncertainties in the initial relative cavity depth $1.3 < h/L_0 < 4$, corresponding in experiment to initial separations of just 0.25–0.75 mm for a cavity depth of $h = 1$ mm. The plateaus in the experiment at the highest Ca are likely artifacts of operating the apparatus at its upper limit of speed.

Hereafter, the geometric parameters are fixed to the values in Fig. 2. A systematic sweep over the relevant range of material parameters is summarized in Fig. 4. The Bond number is varied between $-2.4 < \mathrm{Bo} < 2.4$ in Fig. 4a; the effect of inertia is suppressed by setting a high viscosity ($\mathrm{Oh} > 1.6$ and $\mathrm{Re} < 0.5$). In Fig. 4b, the Bond number is fixed to $\mathrm{Bo} = +1.2$ and the Ohnesorge number is varied in the range $0.03 < \mathrm{Oh} < 1.13$ ($0.0001 < \mathrm{Re} < 200$).

In the limit $\mathrm{Ca} \to 0$, the free surface profile evolution can be approximated as a progression of pseudo-equilibrium solutions to the Young-Laplace equation (although these equilibrium solutions are not necessarily stable). For $\mathrm{Bo} = 0$, this limit implies that the free surface is always symmetric about the mid-plane, leading

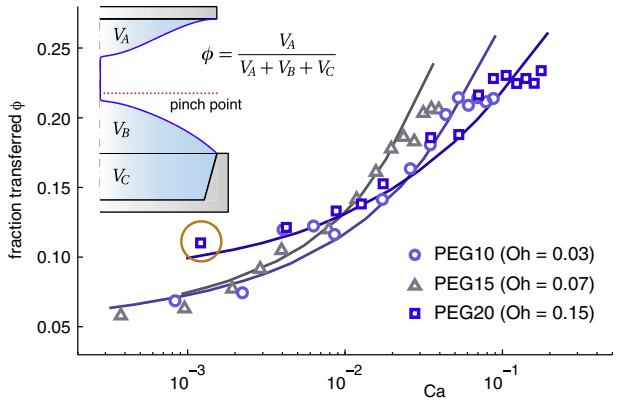

Fig. 3. Fraction ϕ of Newtonian liquid transferred with respect to dimensionless stretching velocity Ca for liquids with $0.03 < Oh < 0.15$ ($0.004 < Re < 20$) and Bo = +1.2, corresponding to aqueous solutions of low molecular weight PEG (solid curves are computed; open symbols are experiments taken from [9]). Inset: terminal free surface profile for $Ca = 10^{-3}$ and Oh = 0.15 with schematic representation of how ϕ is calculated.

to symmetric partition of the liquid above the cavity and a limiting final liquid transfer fraction ϕ^0 (which is not half because of the cavity volume; see Fig. 3 inset). The computed results for Bo = 0 are consistent with this limiting ϕ^0 as indicated in Fig. 4a.

For finite Ca, the process is no longer in the pseudo-equilibrium limit, and Fig. 4a shows that ϕ depends on Ca even in the pseudo-steady limit $Oh \to \infty$ ($Re \to 0$). With increasing Ca, the free surface recedes into the cavity progressively more severely during early times (Fig. 4b). The resulting asymmetric free surface curvature about the mid-plane sets up an adverse capillary pressure gradient that drains liquid back toward the cavity. The competition between this viscous pull-out and associated capillary drainage effect manifests as a minimum in ϕ at $Ca \approx 0.01$.

The cases where $Bo \neq 0$ (negligible inertial effects; $Oh > 1$) are also shown in Fig. 4a, where gravity clearly dominates the overall transfer of liquid, enhancing it when the cavity is above the disk and vice versa. The effect is most dramatic in the $Ca \to 0$ limit where viscous pull-out (and therefore capillary drainage) is inactive. When active at higher Ca, the capillary drainage evidently acts always against both gravity and viscous pull-out, and again results in a minimum ϕ at some critical Ca (whose value depends on Bo). Conversely when $Bo > 0$, gravity and capillary drainage are cooperative and dominate viscous pull-out in the relevant range of Ca; thus ϕ increases monotonically with Ca over the entire range considered.

As Oh is decreased and inertial forces become more important, the stretching liquid filament can develop two pinch points, leading to satellite drop formation (see also Ref. [14]). This drop contains an increasingly significant fraction of the total liquid volume as both Ca increases and Oh decreases, and therefore contributes increasingly to apparent liquid transfer. When Bo = +1.2, decreasing Oh enhances the final liquid transfer at any Ca (Fig. 4c); liquid transfer increases monotonically with both increasing Ca and decreasing Oh. When Bo = −1.2, however, the interactions are more complex and do not lead to a monotonic effect on liquid transfer (Fig. 4d). Results are expected to converge as $Oh \to \infty$, and are practically indistinguishable when $Oh > 0.57$ at which point inertia appears to be effectively suppressed.

In summary, gravity and surface tension dominate liquid transfer at low capillary numbers where both inertial and viscous effects are negligible. At intermediate capillary number when stretching-induced flow is appreciable, capillary effects drain liquid into the cavity. Gravity competes with this drainage when the cavity is

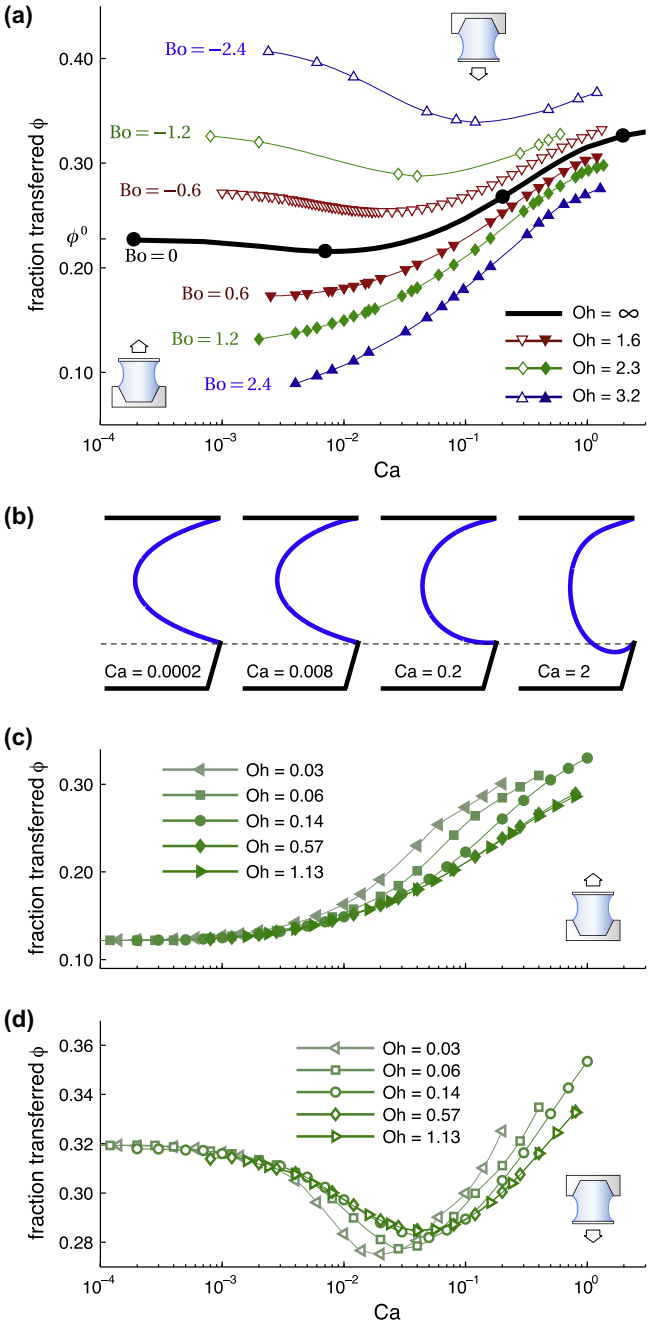

Fig. 4. Summary of Newtonian liquid results with fixed geometry. (a) Varying Bo by altering surface tension at fixed viscosity; Oh is not constant, as shown in legend. $Bo < 0$ denotes experiments inverted in gravity. (b) Free surface profiles for the limiting case Bo = 0 and $Oh = \infty$ at four values of Ca as indicated; profiles are shown at fixed axial strain $L/L_0 = 3.7$. (c) and (d) Varying Oh ($0.0001 < Re < 200$) fixing Bo = +1.2 and Bo = −1.2, respectively. The results for $Oh > 0.57$ ($Re < 3$) are indistinguishable in (c) and (d), indicating that inertia can be neglected in these cases.

on top, resulting in a critical capillary number for minimal liquid transfer. At high capillary number, viscous forces pull more liquid out of the cavity, enhancing liquid transfer. As Fig. 4c shows for $Bo > 0$, liquid transfer is further enhanced as Oh is lowered and inertial effects become stronger (although this generalization is not true when $Bo < 0$). Depending on the relative importance of gravity, systems with high inertia also tend to produce large satellite drops; these can be avoided by restricting attention to high Oh liquids.

3.2. Viscoelastic liquids

The results of Fig. 4c and d indicate that for a fixed Bond number and geometry, experiments with Newtonian liquids are practically equivalent when Oh > 0.57. The viscoelastic PEO solutions used in experiments correspond to Oh = 0.48 and Oh = 0.65, and we therefore fix Oh = 0.57 to compute liquid transfer of viscoelastic liquids. The extensibility parameter is fixed to $b = 50$ for simplicity, and only the Deborah number De and solvent viscosity ratio β are varied.

The effects of varying De fixing $\beta = 0.6$ and Bo = +1.2 are shown in Fig. 5. For comparison to the Newtonian liquid at the same Oh and Bo, fraction liquid transferred ϕ is plotted against Ca. Two effects of viscoelasticity are readily apparent from Fig. 5: (1) elasticity decreases liquid transfer for all Ca and De in the range considered, and (2) there is an optimal capillary number Ca* for maximal liquid transfer. Both of these results are consistent with the findings of Sankaran and Rothstein [9], which are also shown for comparison. Agreement is good for the De ~ 2.9 liquid, but computations could not be reliably carried out for De > 5 due to the well-known numerical difficulties associated with high elasticity flows. The experimentally obtained ϕ appear not to asymptote to the same limiting value as Ca → 0, suggesting either uncertainties in the initial separation L_0 or possibly detachment of the liquid from the translating disk.

Fig. 6a shows the effect of varying the solvent viscosity ratio β with fixed De = 2.0. It is expected that lower β (higher elastic contribution to the total liquid stress) will have the same effect as increasing De; indeed, both decrease overall liquid transfer and shift the optimal Ca* to lower values. Conversely when Bo = −1.2, liquid transfer is enhanced with increasing elasticity (Fig. 6b); this trend was found also in experiments [9]. In a few experimental cases, the contact line on the cavity was observed to de-pin from the corner, additionally enhancing liquid transfer. Although our computations are restricted to pinned contact line, the results of Fig. 6b show that the elastic effect is significant enough to account for most of the enhanced cavity emptying. Similar plots varying 0.2 < De < 5.0 show that the influence of β on liquid transfer is increasingly dramatic with increasing De (see Supplementary materials).

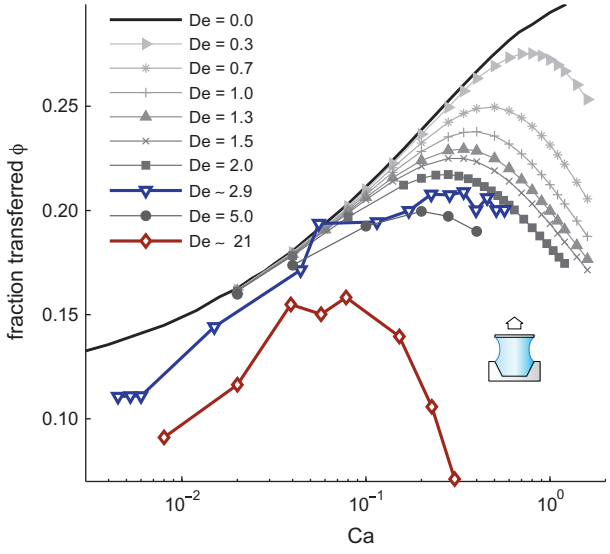

Fig. 5. Effect of varying De at fixed $\beta = 0.6$ on the transfer of a FENE-P liquid with comparison to experimental results [9] (open symbols; assumed $\beta \approx 0.8$). In all cases, Bo = +1.2 and Oh = 0.57.

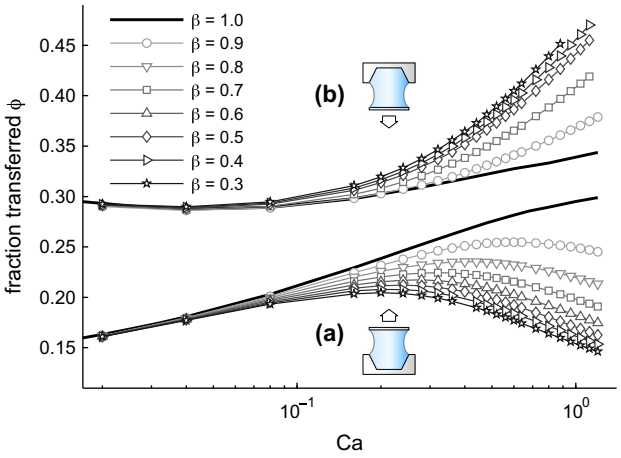

Fig. 6. Effect of varying solvent viscosity ratio β on the transfer of a FENE-P liquid with fixed De = 2.0. The bottom set of curves (a) are for Bo = +1.2, and the top set of curves (b) are for Bo = −1.2 (inverted geometry).

4. Discussion

The main observations of viscoelastic liquid transfer are (1) the exacerbation of gravitational drainage, and (2) that of an optimal coating speed for maximum liquid transfer when Bo > 0 (i.e., when gravity opposes liquid transfer). Below, we discuss these observations in three parts. The first part splits the process into regimes and demonstrates that although final liquid transfer is ultimately determined at late times, there is always an adverse elastic effect activated at early times for high Ca, independently of gravity. The second part defines a Weissenberg number Wi based on the premise that the optimal liquid transfer observed in the Bo > 0 cases occurs at a critical value Wi*. The third part explores quantitatively the transition at this critical Wi* beyond which the early-time elastic effects are activated, in particular examining the change in development of the elastic stress and the deformation of the free surface.

4.1. Process regimes during liquid transfer

The results of Figs. 5 and 6 taken together indicate that the most apparent effect of elasticity is to assist gravitational drainage. This drainage is dominant at late times when the axial displacement L of the disk is high; Sankaran and Rothstein [9] explain this in terms of the extensional strain rate due to stretching $\dot{\varepsilon} = U/L$, which decays as L increases. It follows that liquids with higher elasticity are affected more by gravitational drainage simply because they form thicker liquid bridges, entrapping a larger fraction of the total liquid at the onset of the thinning regime; this is consistent with the observations. To illustrate, a useful quantity to consider is the transient liquid partition ψ, which is defined as the partition of liquid above the principal pinch point at any time during the process so that $\psi|_{\text{break}} = \phi$. In Fig. 7, this quantity is plotted against the scaled axial strain for a FENE-P liquid at two values of Ca.

From Fig. 7, the process can be split into three regimes. The behaviors of Newtonian and FENE-P liquids are qualitatively similar during the early regime I, although elastic effects appear to generally suppress liquid transfer especially in Fig. 7a. Regime II marks the onset of gravitational drainage as determined by the downturn in ψ for the Newtonian liquid when Bo > 0. More importantly at regime II, Fig. 7a shows for FENE-P liquids a sudden reduction in ψ for both Bo cases. At late times denoted regime III, gravity clearly dominates liquid partition, reversing the regime II effect for the Bo < 0 case and enhancing it otherwise.

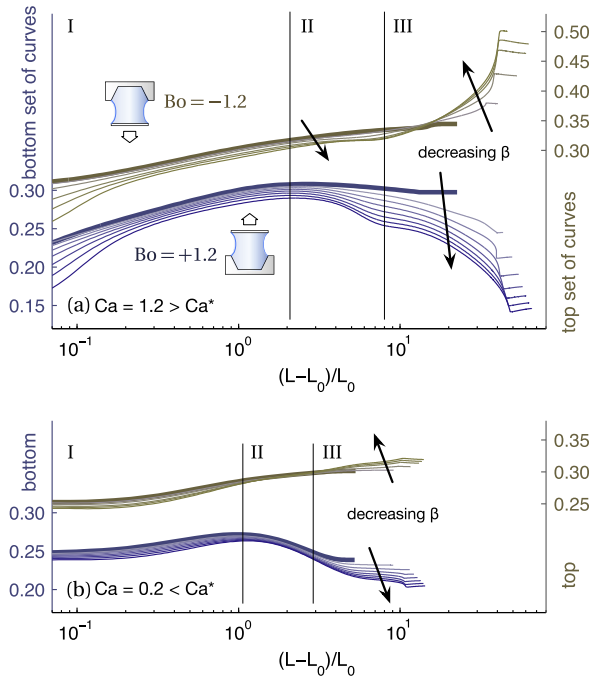

Fig. 7. Transient liquid partition ψ with respect to axial strain for a FENE-P liquid with De = 2.0 and $0.3 < \beta < 0.9$ at (a) Ca = 1.2 and (b) Ca = 0.2. From Fig. 6a, $0.2 < Ca^* < 0.7$ depending on the value of β. The bottom sets of curves is for Bo = +1.2, and the top sets for Bo = −1.2. Bolded curves indicate the Newtonian limit $\beta = 1$.

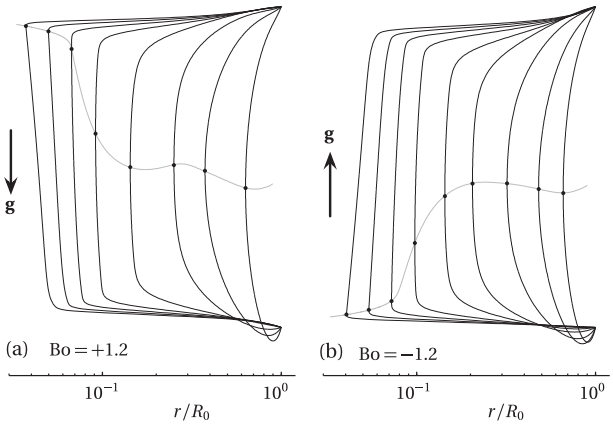

Fig. 8. Comparison between the (a) Bo = + 1.2 and (b) Bo = −1.2 cases of free surface profile evolutions for FENE-P liquid with De = 2.0 and $\beta = 0.4$. Stretching conditions are such that Ca = 0.56 > Ca* (see Fig. 6a). The time between profiles is chosen only for visual clarity. A gray curve tracks the pinch point.

The sudden reduction of ψ in regime II intensifies with decreasing β, indicating that it is a viscoelastically induced drainage. While its effect is obscured in Fig. 6b when Bo < 0, Fig. 7a suggests that the same adverse effect is at work during regime II regardless of the action of gravity. The effect is unobservable in Fig. 7b where Ca < Ca* (for most values of β). Thus, viscoelastically induced drainage in regime II is evidently activated only beyond a critical stretching velocity.

At late times (regime III), elastic effects evidently exacerbate gravitational drainage even when the regime II effect is not activated (Fig. 7b), and indeed this effect eclipses the regime II effect (it is reversed in the Bo < 0 case; Fig. 7a). This result is perhaps surprising in light of the small local Bond numbers $Bo_L = \rho g r^2_{pinch}/\sigma$ associated with the liquid filament at late times: the filament is thin and therefore the local curvature and capillary pressure are high compared to the weight of the filament. However, the relevant quantity to compare against gravitational potential is the gradient of capillary pressure, which is low for nearly cylindrical filaments with nearly constant curvature (zero for perfectly cylindrical filaments). Fig. 8 shows the free surface profile evolutions of a FENE-P liquid with gravity acting in opposite directions, and demonstrates that gravity induces sagging even for local Bond numbers as low as $Bo_L = 5 \times 10^{-3}$.

With increasing Ca, viscous stretching dominates over capillary drainage and leads to more persistent liquid filaments, which are more susceptible to the late time gravitational drainage. Filament persistence is also more prominent with increasing elasticity due to extension-thickening. These observations are consistent with the increasingly dramatic effects (whether enhancement or reduction) on liquid transfer shown in Figs. 5 and 6 when Ca, De, or $(1-\beta)$ are increased.

Computations were also carried out in the limiting case of Bo = 0 with all other dimensionless parameters fixed, and the results are presented as Supplementary materials. In brief, the late time dynamics exhibit the formation of beads-on-a-string structures (see also Refs. [53,54]), and lead to a more complex dependence of final liquid transfer on Ca. Importantly, the results together with those in Fig. 7 confirm that although final liquid transfer fraction is ultimately governed by the details of late time dynamics, there is an elastically induced suppression effect at early times when the disk separation velocity exceeds some critical value.

4.2. Weissenberg number governing liquid transfer suppression

In the absence of elasticity, Fig. 4 shows that liquid transfer for Bo > 0 increases monotonically with coating speed (Ca). The observation that viscoelastic liquids exhibit optimal coating speeds Ca* (Figs. 5 and 6a) together with the results of Fig. 7, suggests that early-time elastic effects are activated only if process strain rates are sufficiently intense. The appropriate dimensionless coating speed must therefore take the form of a Weissenberg number $Wi = \lambda\dot{\gamma}$, comparing the polymer's relaxation time λ to a characteristic strain rate for the relevant process dynamics $\dot{\gamma}$.

Sankaran and Rothstein [9] defined a Weissenberg number in terms of the transient stretching rate U/L. Noting that stretching dynamics are strongest when $L = L_0$, the extensional Weissenberg number is defined as $Wi_\varepsilon = \lambda U/L_0$. However, it is evident from Fig. 5 that the optimal Wi^*_ε depends on De, suggesting that it is not the appropriate scaling that governs optimum liquid transfer. Considering the dependence of Ca* on De and β in Figs. 5 and 6a, we find an empirical scaling for the Weissenberg number

$$Wi = Ca^2 De(1-\beta) = \lambda \frac{U}{R_0}(1-\beta)\cdot\frac{\eta_0 U}{\sigma} \tag{15}$$

The scaling of Eq. (15) is used to recast in Fig. 9a the results of Fig. 5. Normalizing by the optimal liquid transfer fraction, all computed and experimental [9] results over the range $0.2 < De < 21$ and $0.2 < \beta < 0.9$ (fixing Oh, Bo, and geometry) collapse well onto a master curve as shown in Fig. 9b. The experimental data were scaled assuming a value of $\beta = 0.8$, based on shear rheometry revealing that the polymeric contribution is not strong enough to induce significant shear thinning [9].

Importantly, Eq. (15) does not depend on the imposed extension rate U/L_0 but rather on the imposed shear rate U/R_0 (the capillary number can also be interpreted as the comparison of this shear rate to the viscous time scale). Fig. 10 demonstrates that the optimal Weissenberg number does not change with initial liquid bridge aspect ratios $0.12 < L_0/R_0 < 0.6$, further suggesting that the relevant dynamics are that of shear rather than extension.

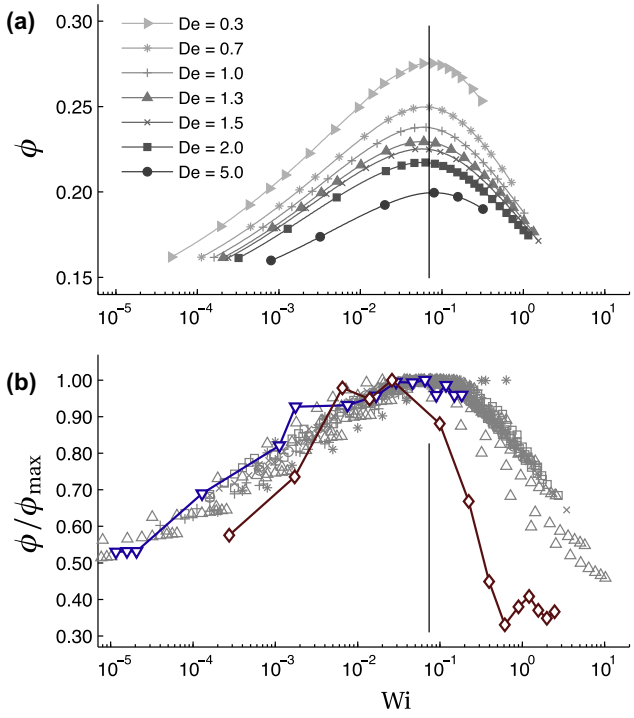

Fig. 9. Fraction of liquid transferred (normalized) with respect to Weissenberg number (Eq. (15)) for all computations with Bo = +1.2 and Oh = 0.57 varying $0.2 < \beta < 0.9$ and $0.2 < De < 5.0$. Bold symbols connected by lines are experimental data [9] with an assumed $\beta = 0.8$: triangles represent short chain PEO solutions with De = 2.9; diamonds represent longer chain PEO solutions with De = 21.5.

Additional explorations of the proposed scalings in Eq. (15) are presented in the Supplementary materials. In brief, the results are confirmed to be independent of Oh (inertia is already negligible), the results appear relatively insensitive to doubling the extensibility parameter b, and most of the spread in Fig. 9 is shown to be due to small values of the term $(1-\beta)$.

The Weissenberg number in Eq. (15) is thus representative of the early-time shear-dominated stretching flow regime and not of the late-time extension-dominated thinning flow regime. The relevant process strain rate $\dot{\gamma}$ includes Ca, indicating that the dynamics are governed by an interaction of elastic, viscous, and capillary forces.

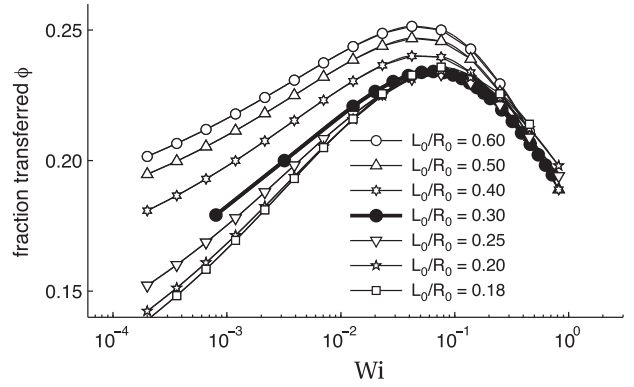

Fig. 10. The initial liquid bridge aspect ratio L_0/R_0 has little effect on the critical Weissenberg number for optimal liquid transfer, indicating that the extension rate U/L_0 is not the relevant strain rate. Liquid transfer fraction ϕ increases with L_0/R_0 because the total amount of liquid above the cavity is also increasing.

4.3. Elastic stress activation near the critical Weissenberg number

The critical Weissenberg number $Wi^* \approx 0.1$ marks the optimal coating speed for maximal liquid transfer when Bo > 0; no such optimum is apparent when Bo < 0. Here we demonstrate that Wi^* marks a transition where elasticity become important relative to the early-time shear. Viscoelastic extension-hardening dominates only at later times, prolonging the life of the filament and providing opportunity for other forces to determine final liquid transfer.

Liquid transfer is proximally governed by the free surface profile evolution, which is in turn governed by Eqs. (11) and (12). Thus, a principal quantity in determining the characteristics of viscoelastic liquid transfer is the dimensionless elastic contribution to the free surface normal stress

$$\tau_e^{fs} = \left(\frac{R_0}{\sigma}\right)\mathbf{nn} : \boldsymbol{\tau}_e \tag{16}$$

where $\mathbf{n}$ is the outward normal to the free surface and $\boldsymbol{\tau}_e$ is the elastic contribution to the total stress. It is made dimensionless by the characteristic stress scale σ/R_0, which is the capillary pressure jump across the free surface at the initial equilibrium configuration without the influence of gravity. Although this characteristic stress does not contain the viscosity η_0, it is equivalent to the viscous stress scale when the characteristic velocity is defined in terms of the initial liquid bridge radius R_0 and viscous time scale t_v. The complete space-time evolution of τ_e^{fs} for a specific set of material parameters is illustrated in Fig. 11, along with free surface profiles at selected time steps.

A series of free surface normal elastic stress evolutions with increasing Wi is shown in Fig. 12. The behavior of τ_e^{fs} changes qualitatively at the critical Weissenberg number, and the direction of gravity appears relatively inconsequential. When $Wi < Wi^*$, the largest elastic stress grows monotonically in the late-time regime due to strong extensional flow stretching out the polymer in the thinning filament. Conversely, when $Wi > Wi^*$, the near-mid-filament elastic stress peaks at early times; the peak occurs

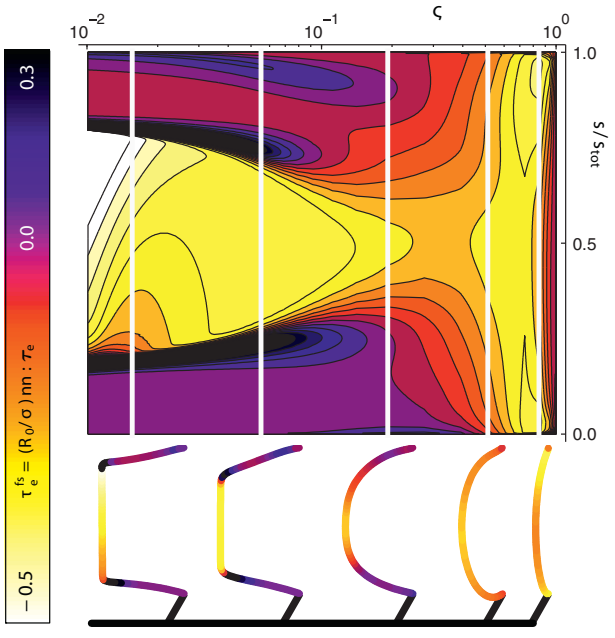

Fig. 11. Contour plot (top) representing the evolution of the free surface normal elastic stress τ_e^{fs} along the interface (s/s_{tot} is the normalized length of arc from the cavity side contact line) with respect to the reduced pinch point radius ς. Negative normal stresses act into the liquid (surface normal is defined as outward pointing). Free surface profiles (bottom) correspond to the vertical slices depicted in the contour plot. The case shown is for De = 1.0, $\beta = 0.6$, and Wi = 0.05.

consistently when the dimensionless pinch point radius achieves a critical value $\varsigma^* \approx 0.3$. This early-time maximum τ_e^{fs} appears at a critical stretching velocity corresponding to $Wi \approx Wi^*$ (Fig. 12), and is representative of elastic effects during the early-time stretching flow regime.

The action of the free surface normal elastic stress is evident also by its influence on the evolution of the free surface, specifically the migration of the dimensionless axial position of the principal pinch point $\chi = z_{pinch}/L$ (shown in Fig. 8 as a locus). Fig. 13 compares the pinch point migration $\chi(\varsigma)$ of the Bo > 0 and Bo < 0 cases over a range of Wi.

When $Wi < Wi^*$, increasing Wi pulls the pinch point toward the cavity, effectively enhancing liquid transfer by partitioning more liquid away from the cavity—this is the same viscous stretching effect illustrated in Fig. 4b with increasing Ca. As Wi increases beyond the optimal Wi^*, the pinch point is pulled increasingly away from the cavity—regardless of the direction of gravity—impeding liquid transfer. The effect is illustrated by plotting against Wi the rate of pinch point migration at the critical pinch point radius $d\chi/d\varsigma|_{\varsigma^*}$ (Fig. 14). Before activation of the elastic stress, pinch point migration is unaffected by increasing Weissenberg number and $d\chi/d\varsigma|_{\varsigma^*} \approx 0$. The downturn in $d\chi/d\varsigma|_{\varsigma^*}$ indicates activation of the elastic effect, and occurs at $Wi \approx Wi^*$ as expected. Fig. 14 further demonstrates that the action is independent of gravity for all computed cases.

Because the early-time elastic suppression and free surface normal elastic stress development has been shown to be independent of the gravitational asymmetry, it must be attributed to the asymmetry associated with the cavity. To probe the influence of the cavity, liquid transfer is calculated for Newtonian and FENE-P liquids (Oh = 0.57, Bo = + 1.2, De = 2, β = 0.5) fixing Ca = 1 and varying cavity wall angle α (Fig. 15). The liquid transfer fraction ϕ for Newtonian liquids decreases with increasing cavity angle because the cavity volume increases (fixed cavity volume computations cannot be carried out of a large range of α due to geometric restrictions). The free surface recedes more strongly into the cavity as the wall angle is made steeper (insets in Fig. 15) analogously to increasing Ca for a fixed geometry. In fact, the fraction of liquid transferred relative to the initial liquid bridge volume (which is the same regardless of the cavity volume) increases with α, indicating that the same viscous pull-out effect illustrated in Fig. 4b is at work.

As expected, the FENE-P liquid exhibits decreased liquid transfer for all α compared to the Newtonian liquid. More importantly, the reduction of liquid transfer relative to the Newtonian limit $(\phi^{Newt} - \phi^{FENE\text{-}P})/\phi^{Newt}$ increases with increasing α (right axis in Fig. 15). This result—namely that the severity of early-time elastic drainage increases with increasing wall angle α—suggests that the elastic free surface normal stress development is intimately related to the early-time free surface recession into the cavity.

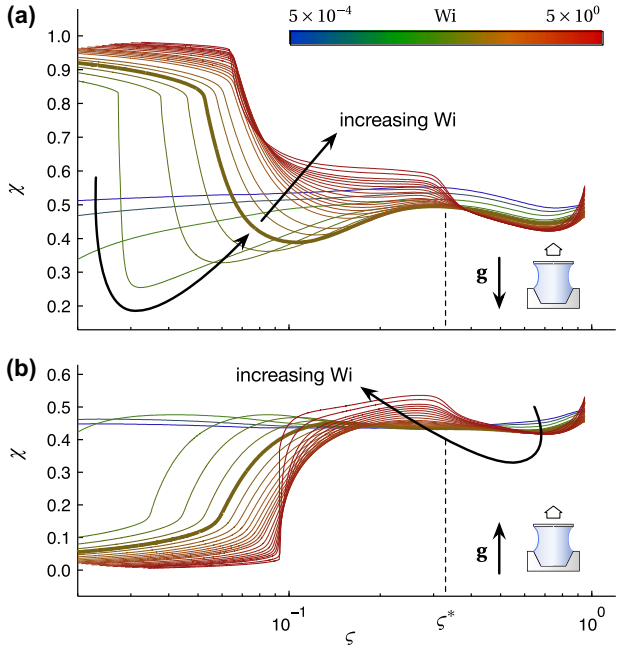

Fig. 13. Migration of the dimensionless axial pinch point location χ (on the cavity side $\chi = 0$) with respect to the pinch point radius ς as a proxy for time (see Fig. 8). The viscoelastic properties are fixed to De = 2.0 and β = 0.4. Upward pinch point migration indicates partitioning of liquid toward the cavity (adverse drainage).

The relationship is further demonstrated by the Ca term in Eq. (15), inasmuch as Ca was shown in Fig. 4b to govern free surface recession during the stretching regime. In other words, increasing either α (steepening cavity walls) or Ca enhances the early-time adverse elastic stress. Conversely, $\alpha = 0$ corresponds to the flat disk (no cavity) case and Ca = 0 corresponds to the pseudo-equilibrium limit, both of which prevent free surface recession into the cavity and therefore the asymmetric elastic stress development that ultimately hinders liquid transfer. Accordingly, the early-time elastic stress should be less important at small Ca, even as $Wi > Wi^*$. Indeed, additional computations (Supplementary materials) varying De at fixed Ca demonstrate that the elastically induced

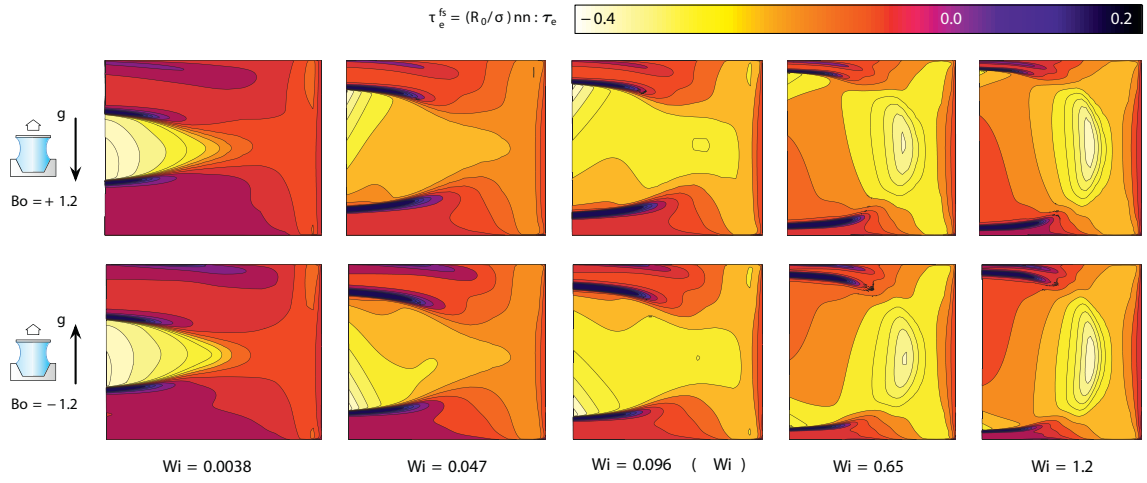

Fig. 12. Free surface normal elastic stress evolution with increasing Wi at fixed De = 2.0 and β = 0.7. The time evolution transitions qualitatively in behavior at $Wi^* \approx 0.1$ regardless of the direction of gravity. The vertical axes are oriented as indicated by the cartoon.

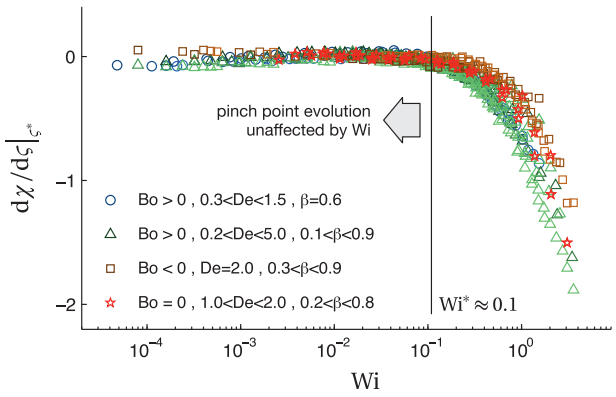

Fig. 14. Summary of elastic activation for all computed results with conditions in the figure legend. The elasticity-activated pull on the free surface (as in Fig. 13) is quantified as the rate of pinch point migration $d\chi/d\varsigma$ when $\varsigma = \varsigma^*$. For all the cases computed at various viscoelastic parameters and the direction of gravity, there is a clear transition in the free surface profile evolution at Wi ≈ Wi* in accordance with observations of optimal liquid transfer in Fig. 9.

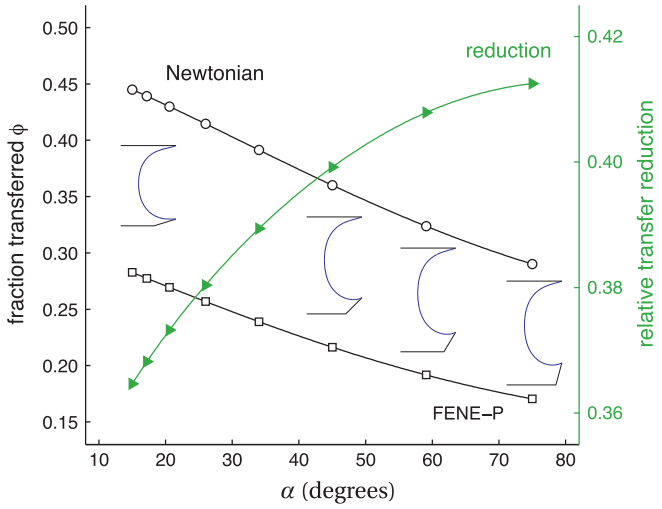

Fig. 15. Liquid transfer (left axis) for Newtonian and FENE-P liquids with Oh = 0.57 and Ca = 1 with varying cavity wall angles α (the cavity vanishes in the limit $\alpha \to 0$; see Fig. 2). Newtonian liquid transfer fraction decreases with increasing α because the cavity volume increases (L_0/R_0 is held constant). For the FENE-P liquid, De = 2 and $\beta = 0.5$. The relative reduction in liquid transfer for the FENE-P liquid $(\phi^{\text{Newt}} - \phi^{\text{FENE-P}})/\phi^{\text{Newt}}$ (right axis) increases with increasing α.

reduction of liquid transfer with respect to Wi diminishes with decreasing Ca.

5. Conclusion

This study examined computationally the role of viscoelasticity on liquid transfer during a model gravure process with the pinned contact line condition. We computed the fractions of Newtonian and FENE-P liquids transferred from an axisymmetric cavity to a disk as a function of the disk's axial displacement velocity, and demonstrated quantitative agreement between computations and earlier experiments [9].

With increasing disk velocity, strong free surface normal elastic stresses develop at early times and act to pull liquid back into the cavity. This action is always adverse to liquid transfer, independent of gravity, and is governed by the early-time stretching dynamics where flow is dominated by shear. The final fraction of transferred liquid is decided ultimately during the late-time extension-dominated thinning regime where viscoelastic extension-hardening delays filament break-up and allows prolonged drainage, gravitational or otherwise. In the case where gravity reinforces the early-time viscoelastic drainage, the competition with viscous forces manifests as an optimal disk velocity corresponding to a critical Weissenberg number.

Because a typical gravure cell is smaller than our model system as measured by the Bond number, gravity will be less important in a real system. According to the adverse elastic effects activated at the critical Weissenberg number, the practical implication for a real gravure coating or printing process with viscoelastic liquid is the existence of an operating window for coating speed. This window shifts to lower speeds with increasing polymer relaxation time (higher molecular weight polymer) or increasing elastic contribution to the zero-shear viscosity (higher polymer concentration in the liquid). Without significant gravity, however, the stretching viscoelastic liquid filament may break up into satellite drops (misting defect). The details of this late time behavior may ultimately enhance or reverse the early-time elastic suppression effect to determine the final efficiency of liquid transfer. More studies are therefore needed to understand the late time behavior of persistent liquid filaments during gravure processes, especially regarding the formation of beads-on-a-string.

Further investigations should also explore the effect of applying a more realistic model for the separation of the cavity and disk—the constant acceleration model works well at small separations. In such cases, absolute motions of the cavity and disk, which essentially models the angle of departure of the web from the gravure roll, will be important for low Ohnesorge number liquids due to inertial effects.

A more complete model for gravure requires a systematic investigation of viscoelastic effects on the de-wetting of liquid undergoing extension from a gravure cavity. Observing the contact line is challenging in experiments due to the cavity geometry [9]. Computing de-wetting viscoelastic flows requires modeling the contact line physics—which are still poorly understood—and more robust numerical methods to reconcile outstanding issues that arise when modeling both viscoelasticity and dynamic (de)-wetting. Once these challenges are overcome, computations promise to complement the ongoing efforts in understanding the role of complex rheology and interfacial phenomena in gravure processes.

Acknowledgements

This work was supported by an NSF NSEC under Grant Nos. CMMI-0531171 and CMMI-1025020. Computations were supported in part by the Data Analysis and Visualization Cyberinfrastructure funded by NSF under Grant OCI-0959097; by NIH award NCRR S10RR02950 and an IBM Shared University Research (SUR) Award in partnership with CISCO, Qlogic and Adaptive Computing; and by the Shared University Grid at Rice funded by NSF under Grant EIA-0216467, and a partnership between Rice University, Sun Microsystems, and Sigma Solutions, Inc.

Appendix A. Supplementary material

Supplementary data associated with this article can be found, in the online version, at http://dx.doi.org/10.1016/j.jnnfm.2013.05.005.

References

[1] M. Pudas, J. Hagberg, S. Leppavuori, The absorption ink transfer mechanism of gravure offset printing for electronic circuitry, IEEE Trans. Electronics. Pack. Manuf. 25 (2002) 335–343.
[2] F.C. Krebs, Fabrication and processing of polymer solar cells: a review of printing and coating techniques, Solar Energy Mater. Solar Cells 93 (2009) 394–412.

[3] X. Yin, S. Kumar, Flow visualization of the liquid emptying process in scaled-up gravure grooves and cells, Chem. Eng. Sci. 61 (2006) 1146–1156.
[4] T.-M. Lee, S.-H. Lee, J.-H. Noh, D.-S. Kim, S. Chun, The effect of shear force on ink transfer in gravure offset printing, J. Micromech. Microeng. 20 (2010) 125026.
[5] N. Hoda, S. Kumar, Boundary integral simulations of liquid emptying from a model gravure cell, Phys. Fluids 20 (2008) 092106.
[6] C.A. Powell, M.D. Savage, P.H. Gaskell, Modelling the meniscus evacuation problem in direct gravure coating, Chem. Eng. Res. Des. 78 (2000) 61–67.
[7] S. Reddy, P.R. Schunk, R.T. Bonnecaze, Dynamics of low capillary number interfaces moving through sharp features, Phys. Fluids 17 (2005) 122104.
[8] S. Dodds, M.d.S. Carvalho, S. Kumar, The dynamics of three-dimensional liquid bridges with pinned and moving contact lines, J. Fluid Mech. 707 (2012) 521–540.
[9] A.K. Sankaran, J.P. Rothstein, Effect of viscoelasticity on liquid transfer during gravure printing, J. Non-Newtonian Fluid Mech. 175–176 (2012) 64–75.
[10] H.W. Kang, H.J. Sung, T.-M. Lee, D.-S. Kim, C.-J. Kim, Liquid transfer between two separating plates for micro-gravure-offset printing, J. Micromech. Microeng. 19 (2008) 015025.
[11] H.K. Chuang, C.C. Lee, T.J. Liu, An experimental study on the pickout of scaled-up gravure cells, Intern. Polym. Process. XXIII (2008) 216–222.
[12] C.A. Powell, M. Savage, J. Guthrie, Computational simulation of the printing of Newtonian liquid from a trapezoidal cavity, Int. J. Numer. Heat Fluid Flow 12 (2002) 338–355.
[13] S. Dodds, M.d.S. Carvalho, S. Kumar, Stretching and slipping of liquid bridges near plates and cavities, Phys. Fluids 21 (2009) 092103.
[14] S. Dodds, M.d.S. Carvalho, S. Kumar, Stretching liquid bridges with moving contact lines: the role of inertia, Phys. Fluids 23 (2011) 092101.
[15] F. Ghadiri, D.H. Ahmed, H.J. Sung, E. Shirani, Non-Newtonian ink transfer in gravure-offset printing, Int. J. Heat Fluid Flow 32 (2011) 308–317.
[16] W.-X. Huang, S.-H. Lee, H.J. Sung, T.-M. Lee, D.-S. Kim, Simulation of liquid transfer between separating walls for modeling micro-gravure-offset printing, Int. J. Heat Fluid Flow 29 (2008) 1436–1446.
[17] L. Rayleigh, On the instability of jets, Proc. London Math. Soc. 10 (1878) 4–13.
[18] J.A.F. Plateau, Experimental and theoretical researches on the figures of equilibrium of a liquid mass, Annu. Rep. Smithsonian Inst. (1863).
[19] J. Eggers, Universal pinching of 3D axisymmetric free-surface flow, Phys. Rev. Lett. 71 (1993) 3458–3460.
[20] J. Eggers, Nonlinear dynamics and breakup of free-surface flows, Rev. Mod. Phys. 69 (1997) 865–930.
[21] D. Papageorgiou, On the breakup of viscous liquid threads, Phys. Fluids 7 (1995) 1529–1544.
[22] M. Renardy, A comment on smoothness of viscoelastic stresses, J. Non-Newtonian Fluid Mech. 138 (2006) 204–205.
[23] R. Gillette, D. Dyson, Stability of fluid interfaces of revolution between equal solid circular plates, Chem. Eng. J. 2 (1971) 44–54.
[24] X. Pepin, D. Rossetti, S.M. Iveson, S.J.R. Simons, Modeling the evolution and rupture of pendular liquid bridges in the presence of large wetting hysteresis, J. Colloid Interface Sci. 232 (2000) 289–297.
[25] B. Qian, K.S. Breuer, The motion, stability and breakup of a stretching liquid bridge with a receding contact line, J. Fluid Mech. 666 (2011) 554–572.
[26] T. Sridhar, V. Tirtaatmadja, D.A. Nguyen, R.K. Gupta, Measurement of extensional viscosity of polymer solutions, J. Non-Newtonian Fluid Mech. 40 (1991) 271–280.
[27] V. Tirtaatmadja, T. Sridhar, Comparison of constitutive-equations for polymer-solutions in uniaxial extension, J. Rheol. 39 (1995) 1133–1160.
[28] P. Szabo, Transient filament stretching rheometer I: force balance analysis, Rheol. Acta 36 (1997) 277–284.
[29] S.L. Anna, G.H. McKinley, Elasto-capillary thinning and breakup of model elastic liquids, J. Rheol. 45 (2001) 115–138.
[30] R.W.G. Shipman, M.M. Denn, R. Keunings, Mechanics of the "falling plate" extensional rheometer, J. Non-Newtonian Fluid Mech. 40 (1991) 281–288.
[31] M. Kolte, H.K. Rasmussen, O. Hassager, Transient filament stretching rheometer II: numerical simulation, Rheol. Acta 36 (1997) 285–302.
[32] G.H. McKinley, A. Tripathi, How to extract the Newtonian viscosity from capillary breakup measurements in a filament rheometer, J. Rheol. 44 (2000) 653–670.
[33] S. Gaudet, G.H. McKinley, H.A. Stone, Extensional deformation of Newtonian liquid bridges, Phys. Fluids 8 (1996) 2568–2579.
[34] X. Zhang, R. Padgett, O.A. Basaran, Nonlinear deformation and breakup of stretching liquid bridges, J. Fluid Mech. 329 (1996) 207–245.
[35] P. Doshi, R. Suryo, O.E. Yildirim, G.H. McKinley, O.A. Basaran, Scaling in pinch-off of generalized Newtonian fluids, J. Non-Newtonian Fluid Mech. 113 (2003) 1–27.
[36] P.P. Bhat, O.A. Basaran, M. Pasquali, Dynamics of viscoelastic liquid filaments: low capillary number flows, J. Non-Newtonian Fluid Mech. 150 (2008) 211–225.
[37] D.H. Ahmed, H.J. Sung, D.-S. Kim, Simulation of non-Newtonian ink transfer between two separating plates for gravure-offset printing, Int. J. Heat Fluid Flow 32 (2011) 298–307.
[38] C. Huh, L.E. Scriven, Hydrodynamic model of steady movement of a solid/liquid/fluid contact line, J. Colloid Interface Sci. 35 (1971) 85–101.
[39] T.D. Blake, The physics of moving wetting lines, J. Colloid Interface Sci. 299 (2006) 1–13.
[40] M. Yao, G.H. McKinley, Numerical simulation of extensional deformations of viscoelastic liquid bridges in filament stretching devices, J. Non-Newtonian Fluid Mech. 74 (1998) 47–88.
[41] C. Zhou, P. Yue, J.J. Feng, C.F. Ollivier-Gooch, H.H. Hu, 3D phase-field simulations of interfacial dynamics in Newtonian and viscoelastic fluids, J. Comput. Phys. 229 (2010) 498–511.
[42] P. Yue, J.J. Feng, C. Liu, J. Shen, Diffuse-interface simulations of drop coalescence and retraction in viscoelastic fluids, J. Non-Newtonian Fluid Mech. 129 (2005) 163–176.
[43] P. Yue, J.J. Feng, Phase-field simulations of dynamic wetting of viscoelastic fluids, J. Non-Newtonian Fluid Mech. 189–190 (2012) 8–13.
[44] M. Pasquali, L.E. Scriven, Free surface flows of polymer solutions with models based on the conformation tensor, J. Non-Newtonian Fluid Mech. 108 (2002) 363–409.
[45] M. Pasquali, L.E. Scriven, Theoretical modeling of microstructured liquids: a simple thermodynamic approach, J. Non-Newtonian Fluid Mech. 120 (2004) 101–136.
[46] M. Grmela, P.J. Carreau, Conformation tensor rheological models, J. Non-Newtonian Fluid Mech. 23 (1987) 271–294.
[47] A.N. Beris, B.J. Edwards, Thermodynamics of Flowing Systems with Internal Microstructure, Oxford Engineering Science Series, Oxford University Press, New York, 1994.
[48] R.J.J. Jongschaap, A generic matrix representation of configuration tensor rheological models, J. Rheol. 38 (1994) 769–796.
[49] J.M. de Santos Avila, Two-Phase Cocurrent Downflow Through Constricted Passages, Ph.D. Thesis, University of Minnesota, 1991.
[50] K.N. Christodoulou, L.E. Scriven, Discretization of viscous free surface flows and other free boundary problems, J. Comput. Phys. 99 (1992) 39–55.
[51] A.N. Brooks, T.J.R. Hughes, Streamline Upwind/Petrov-Galerkin formulations for convection dominated flows with particular emphasis on the incompressivle Navier–Stokes equations, Comput. Meth. Appl. Mech. Eng. 32 (1982) 199–259.
[52] P.M. Gresho, R.L. Lee, R.L. Sani, Recent advances in numerical methods in fluids, Pineridge Press Ltd., 1980.
[53] P.P. Bhat, M. Pasquali, O.A. Basaran, Beads-on-string formation during filament pinch-off: dynamics with the PTT model for non-affine motion, J. Non-Newtonian Fluid Mech. 159 (2009) 64–71.
[54] P.P. Bhat, S. Appathurai, M. Harris, M. Pasquali, G.H. McKinley, O.A. Basaran, Formation of beads-on-a-string structures during break-up of viscoelastic filaments, Nat. Phys. 6 (2010) 625–631.